PHOTONICS Research

On-chip topological transport of integrated optical frequency combs

ZHEN JIANG,[1,2,†] HONGWEI WANG,[1,†] PENG XIE,[3] YUECHEN YANG,[1,2] YANG SHEN,[1,2] BO JI,[1,2] YANGHE CHEN,[1,2] YONG ZHANG,[1] LU SUN,[1] ZHENG WANG,[1] CHUN JIANG,[1,5] YIKAI SU,[1,6] AND GUANGQIANG HE[1,2,4,7]

[1]State Key Laboratory of Advanced Optical Communication Systems and Networks, Department of Electronic Engineering, Shanghai Jiao Tong University, Shanghai 200240, China
[2]SJTU Pinghu Institute of Intelligent Optoelectronics, Department of Electronic Engineering, Shanghai Jiao Tong University, Shanghai 200240, China
[3]School of Electrical & Electronic Engineering, Nanyang Technological University, Singapore 639798, Singapore
[4]State Key Laboratory of Precision Spectroscopy, East China Normal University, Shanghai 200062, China
[5]e-mail: cjiang@sjtu.edu.cn
[6]e-mail: yikaisu@sjtu.edu.cn
[7]e-mail: gqhe@sjtu.edu.cn
[†]These authors contributed equally to this work.

Received 16 August 2024; revised 16 October 2024; accepted 28 October 2024; posted 29 October 2024 (Doc. ID 538355); published 24 December 2024

Optical frequency combs in integrated photonics have widespread applications in high-dimensional optical computing, high-capacity communications, high-speed interconnects, and other paradigm-shifting technologies. However, quantum frequency combs with high-dimensional quantum states are vulnerable to decoherence, particularly in the presence of perturbations such as sharp bends. Here we experimentally demonstrate the robust on-chip topological transport of quantum frequency combs in valley photonic crystal waveguides. By measuring the time correlations and joint spectral intensity of the quantum frequency combs, we show that both quantum correlations and frequency entanglement remain robust against sharp bends, owing to the topological nature of the quantum valley Hall effect. We also demonstrate that dissipative Kerr soliton combs with a bandwidth of 20 THz maintain their spectral envelope and low-noise properties even in the presence of structure perturbations. These topologically protected optical frequency combs offer robust, complex, highly controllable, and scalable light sources, promising significant advances in high-dimensional photonic information processing.

https://doi.org/10.1364/PRJ.538355

1. INTRODUCTION

Integrated optical frequency combs (OFCs) offer a vast number of time and frequency modes, significantly expanding the dimensionality of photonic systems. Due to their distinctive frequency signatures, OFCs have been extensively studied across both classical and quantum domains, encompassing classical dissipative Kerr soliton (DKS) combs and quantum frequency combs (QFCs). Fully coherent DKS combs have wide applications in ultrafast ranging [1–4], optical communications [5], optical spectroscopy [6,7], frequency synthesis [8,9], and optical computing [10,11]. In addition, QFCs operating at the single-photon level can generate high-dimensional quantum states in the frequency domain, enhancing the complexity and scalability of quantum information processing [12–14]. Recent studies have shown that QFCs enable high-dimensional frequency entanglement [15–18], energy-time entanglement [19–23], and time-bin multiphoton entanglement [24], offering promising applications in quantum communication [25] and quantum computation [26]. It is well known that high-dimensional quantum states are susceptible to decoherence in the presence of sharp bends [27,28]. Therefore, a key challenge in quantum information technology is to achieve robustness of high-dimensional quantum states against sharp bends.

In parallel, topological photonics introduces new capabilities for photonic devices, including unidirectional light transport, along with immunity to structural defects [29–37]. Due to the topological protection properties, topological photonics is soon introduced into nonlinear optics and quantum optics, inspiring many significant advances, including the topological harmonic generation [38,39], topological nonlinear imaging [40], topological single-photon and biphoton states [41–43], topological quantum emitters [28], topological frequency combs [44–47], topological quantum interference [48,49], and even topological quantum logic gates [50]. However, the topological protection of high-dimensional quantum states against sharp bends remains unexplored. Valley photonic crystal (VPC) waveguides, which emulate the quantum valley Hall (QVH) effect, exhibit promising characteristics such as broad bandwidth, low transmission loss, and ultra-compact chip sizes [51]. These features open exciting possibilities for achieving robust on-chip topological transport of high-dimensional quantum states with large bandwidths.

Here we experimentally demonstrate the on-chip topological transport of both QFCs and DKS combs in VPC waveguides. Our VPC topological waveguide supports topologically protected kink states with a significant topological bandgap of approximately 25 THz, enabling the topological transmission of OFCs with extremely wide frequency ranges. Using a Si_3N_4 micro-resonator with a free spectral range (FSR) of 100 GHz, we can access QFCs and DKS combs at different pump powers. We measure the coincidence-to-accidental ratio (CAR) and joint spectral intensity (JSI) (in a 5×5 mode subspace) of QFCs, and find that the quantum correlations and frequency entanglement are topologically protected. Additionally, we demonstrate that fully coherent DKS combs, including single-soliton states, multisoliton states, and soliton crystals, maintain their spectral envelope and low-noise features even after traveling through the topological interfaces. Our findings show the potential for topologically protected unidirectional transport of high-dimensional quantum states and phase-locked soliton states, promising new approaches to high-dimensional information processing utilizing topology in classical and quantum optics.

2. RESULTS

A. Design of VPCs

Our topological device supporting the on-chip transport of OFCs is illustrated in Fig. 1(a). The topological waveguides are fabricated using a silicon-on-insulator (SOI) wafer with a silicon layer thickness of 220 nm (see Section 4). The VPCs are composed of a graphene-like lattice with a lattice constant of $a_0 = 433$ nm. Each unit cell comprises two triangular holes with side lengths of d_1 and d_2. For unperturbed unit cells ($d_1 = d_2 = 216$ nm), the C_6 symmetry leads to a degenerated Dirac point at the K and K′ valleys. Breaking the inversion symmetry ($d_1 \neq d_2$) results in a complete bandgap in the Brillouin zone (see Appendix B). It is noted that the eigenmodes at the K and K′ valleys exhibit opposite polarization. The valley Chern numbers of VPC_1 ($d_1 = 122$ nm and $d_2 = 295$ nm) and VPC_2 ($d_1 = 295$ nm and $d_2 = 122$ nm) are calculated as $C_{v1} = -1/2$ and $C_{v2} = 1/2$, respectively (see

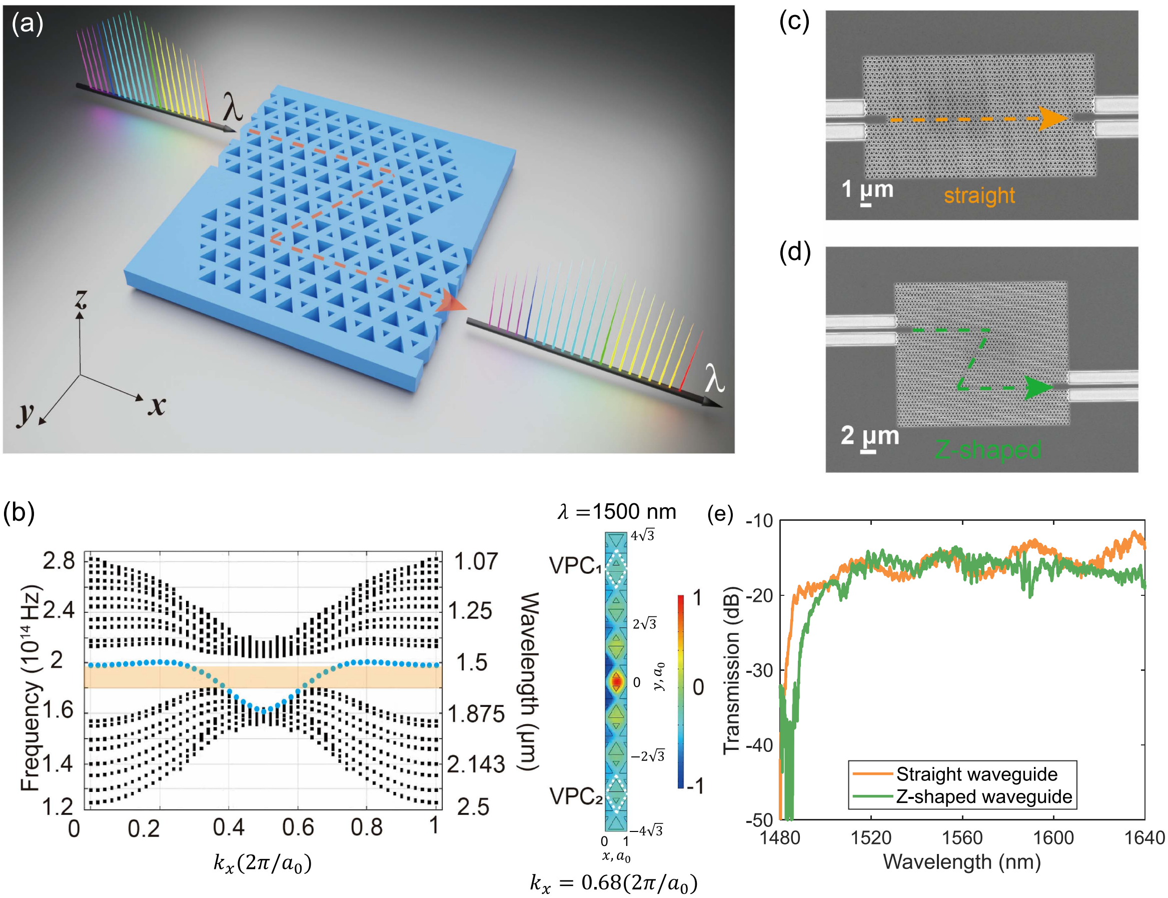

Fig. 1. (a) Scheme of VPC waveguides supporting on-chip topological transport of OFCs. (b) Edge dispersion of the VPCs, where the yellow region denotes the operation bandwidth of the valley kink state. Right panel: H_z field distributions for the topological edge state. SEM images of the (c) straight and (d) Z-shaped topological waveguides. (e) Measured transmission spectra of the straight (orange curve) and Z-shaped topological waveguides (green curve).

Appendix A). At the interface between VPC_1 and VPC_2, the interchange of VPCs reverses the sign of the valley Chern numbers. Note that the difference between the valley indices at the K point across the interface is $\Delta C^K_{\text{edge1}} = C_{v2} - C_{v1} > 0$ [34,52], which determines the propagation direction of the edge state around each valley.

Figure 1(b) shows the calculated edge dispersion of the VPCs. There exists a pair of valley kink states (blue curves) with a bandwidth of approximately 25 THz (highlighted in yellow), spanning from 175 to 200 THz. Importantly, such a large bandwidth allows the topological transport of OFCs with a bandwidth of approximately 200 nm at telecommunication wavelengths. The two valley kink states with opposite group velocities are locked to different valleys, referred to as "valley-locked" chirality [33,34]. The right panel of Fig. 1(b) displays the field distribution for the valley kink state at $k_x = 0.68\pi/a_0$, showing strong localization of electric field around the interface.

To verify robustness against sharp turns, we designed two types of waveguides: straight and Z-shaped topological waveguides [see scanning electron microscopy (SEM) images in Figs. 1(c) and 1(d)]. The in-and-out coupling of the topological waveguides is achieved using lensed fibers, with an insertion loss of 6 dB/face. As shown in Fig. 1(e), the measured transmission spectrum of the Z-shaped waveguide closely matches that of the straight waveguide, indicating that the valley kink states are robust against sharp bends. It can clearly be seen that the measured transmission spectra align well with the simulation results (see Appendix B). Due to the cutoff excitation wavelengths of the pump laser, we are only able to access the topological bandgap from 1490 to 1640 nm.

B. Topological Transport of QFCs

Thanks to the large topological bandgap of the valley kink states, we are able to achieve on-chip topological transport of broadband QFCs with frequency entanglement. Our QFC is generated using a Si_3N_4 micro-resonator with a high-quality factor (Q-factor) of 1.68×10^6 (see Appendix C). To manipulate the broadband phase matching for spontaneous four-wave mixing (FWM) processes, we carefully design the waveguide cross-section to achieve weak anomalous group-velocity dispersion [53].

Figure 2 shows the experimental setup for the topological transport of OFCs, with the details provided in Section 4. We pump the Si_3N_4 micro-resonator at below-threshold power around 1550 nm. As a result of the spontaneous FWM process, a two-photon high-dimensional frequency-entangled state, also referred to as a biphoton frequency comb, is generated [14]. The QFCs with a high-dimensional quantum state could significantly increase the capability of quantum information processing [15,24]. Generally, the quantum state of the QFC can be written as [15]

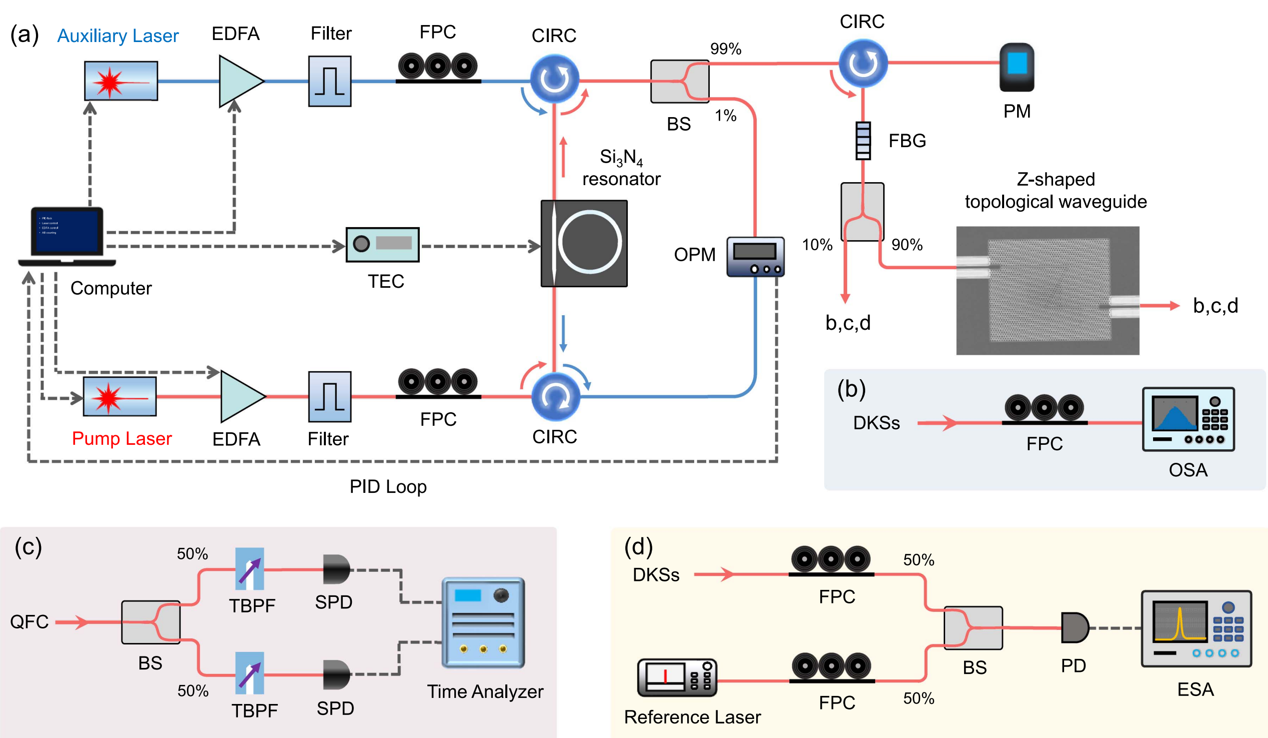

Fig. 2. (a) Experimental setup for topological transport of OFCs. To generate QFCs, the pump laser is actively tuned by a proportional-integral-differential (PID) controller, while the auxiliary laser is not used. To generate DKSs, both lasers are utilized to pump the resonator. EDFA, erbium-doped fiber amplifier; FPC, fiber polarization controller; CIRC, optical circulator; OPM, programable optical power meter; FBG, fiber Bragg grating; OSA, optical spectrum analyzer; ESA, electrical spectrum analyzer; TBPF, tunable bandpass filter; SPD, single-photon detector. (b) Experimental setup for the DKS spectrum measurements. (c) Experimental setup for time correlations and JSI measurements of QFCs. (d) Experimental setup for RF beat notes of the single-soliton states and a CW reference laser.

$$|\Psi\rangle = \sum_{k=1}^{N} \alpha_k |k,k\rangle_{\mathrm{si}}, \quad \text{with} \sum |\alpha_k|^2 = 1, \tag{1}$$

where $|k,k\rangle_{\mathrm{si}}$ is the signal and idler photons for the kth comb line pair, $k = 1, 2, \ldots, N$ is the mode number, and the complex element α_k represents the amplitude and phase of the signal-idler photon pair. The $|k,k\rangle_{\mathrm{si}}$ is given by

$$|k,k\rangle_{\mathrm{si}} = \int \mathrm{d}\Omega \Phi(\Omega - k\Delta\omega)|\omega_p + \Omega, \omega_p - \Omega\rangle_{\mathrm{si}}, \tag{2}$$

in which Ω is the frequency deviation from the pump frequency ω_p, $\Delta\omega$ is the FSR of the resonator, and $\Phi(\Omega)$ is the Lorentzian spectrum function. The quantum state $|k,k\rangle_{\mathrm{si}}$ is a superposition of multiple frequency modes, symmetrically distributed around the pump mode.

Figures 3(a)–3(c) show the measured single-photon spectra at the outputs of the micro-resonator, straight, and Z-shaped topological waveguides, respectively. We observe comb-like spectra with a bandwidth of 80 nm and a mode spacing of approximately 0.8 nm. In our QFC, an individual signal or idler photon forms a coherent superposition of 48 frequency modes, signifying the realization of a quantum system with at least 48 dimensions. Notably, the spectra of the QFCs detected at the output ports of the topological waveguides are nearly identical, indicating that the QFC experiences no significant loss after traversing sharp bends. This observation is consistent with the transmission spectra of the topological waveguides shown in Fig. 1(e).

To confirm the quantum correlation of our QFCs, we record the relative arrival time between correlated photon pairs (S_7I_7) and uncorrelated photon pairs (S_7I_8) as coincidences. Any events involving uncorrelated photon pairs are considered accidental counts, which include dark counts, background counts, and uncorrelated photon counts [20]. We fit the three coincidence peaks using the second-order Glauber correlation function $g_{\mathrm{si}}(\Delta t) \propto \exp(-\Delta t/\tau)$, where τ represents the coherence time of the correlated photons. The fitted coherence times for the three QFCs are 2.90 ns, 2.69 ns, and 2.45 ns, respectively, which align with the resonance linewidth (around 115 MHz). Due to the decoherence of quantum states at sharp corners, the coherence time of the photon pairs is slightly reduced. After transmission through the Z-shaped waveguide, the coherence time decreased by approximately 8.92% compared to that in the straight waveguide. This small degradation

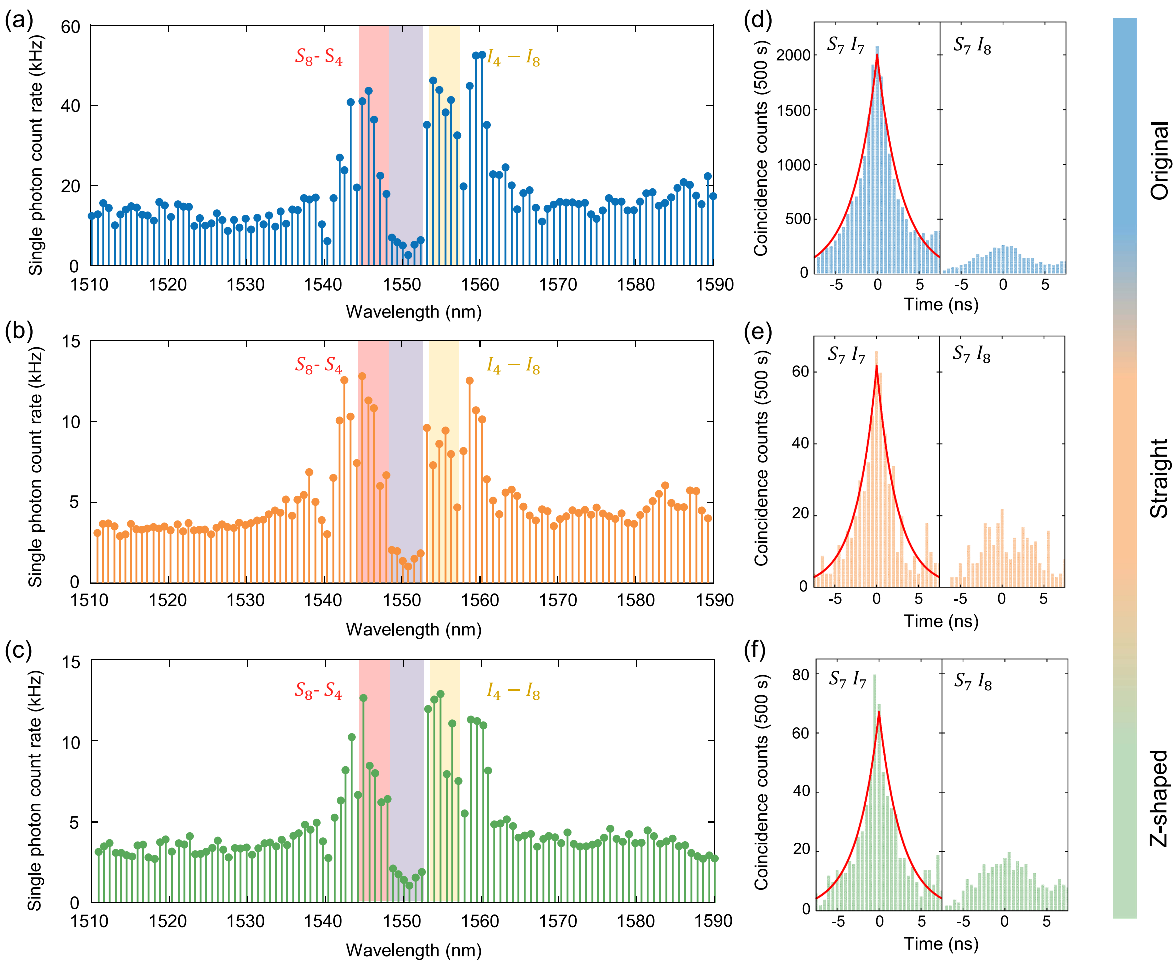

Fig. 3. (a)–(c) Measured single-photon spectra and (d)–(f) signal-idler coincidence histograms of the QFCs at the outputs of the original micro-resonator, straight, and Z-shaped topological waveguides, respectively. The pink, purple, and yellow marked regions denote the selected signal modes, idler modes, and several modes eliminated by the FBG, respectively.

indicates the topological protection of time correlation in the QVH systems. In addition, we obtain CAR values of 9.7, 10.7, and 10.2 from the correlation peaks, respectively. It is worth noting that high on-chip power (6 mW) increases accidental counts, leading to low CAR values. Furthermore, we demonstrate that our topological QFCs can function as wavelength-multiplexed heralded signal-photon sources (see Section 4).

Furthermore, to assess the spectral correlations across the photon-pair spectrum, we measure the JSI distributions for mode-by-mode photon counting, covering five sideband pairs ($S_{4-8}I_{4-8}$). The JSI, which demonstrates spectral correlations, arises from energy and momentum conservation [54]. The results shown in Figs. 4(a)–4(c) clearly reveal the frequency correlation of the signal-idler modes generated through the FWM processes. Only photon pairs that satisfy the energy conservation relation ($2\omega_p = \omega_s + \omega_i$) exhibit strong frequency correlation. We implement a correction for the three JSIs by subtracting the accidental coincidence counts (induced by dark counts, background noise, and after-pulse detection of InGaAs SPDs).

We use Schmidt decomposition to evaluate the frequency entanglement of QFCs [55] (see Appendix E). Figures 4(d)–4(f) show the distributions of normalized Schmidt coefficients λ_n and entanglement entropy S_k for three QFCs, respectively. The Schmit coefficients λ_n represent the possibility of obtaining the nth quantum state, where nonzero Schmidt coefficients (greater than one) indicate the frequency entanglement [55]. The Schmidt numbers $K = \left(\sum \lambda_n^2\right)^{-1}$ and entanglement entropy $S_k = -\sum \lambda_n \log_2 \lambda_n$ are used to demonstrate the presence of two-photon frequency entangled states, where a larger K value indicates higher-quality entanglement [55]. We obtain the entanglement entropy of 1.41, 1.16, and 1.07 for three QFCs, respectively. Moreover, the Schmidt numbers K are calculated as 1.89, 1.63, and 1.53, respectively, which proves the existence of frequency entanglement. By comparing the Schmidt numbers of QFCs at the outputs of straight and Z-shaped topological waveguides, we demonstrate the robustness of frequency entanglement in the presence of sharp bends. Notably, using superconducting nanowire single-photon detectors (SNSPDs) could significantly improve the Schmidt numbers. By filtering out the off-diagonal elements in the measured JSI, we can achieve a Schmidt number greater than 4.0. Such a significant Schmidt number indicates the presence of a quantum state with effective dimensions of $D = 4$. Consequently, this can lead to a topological high-dimensional quantum entangled state, paving the way for intricate, large-scale quantum simulations and computations.

Alternatively, one can evaluate the single-photon purity, which is associated with the factorizability of two-photon quantum states via Schmidt decomposition. Typically, single-photon purity is quantified by $\mathrm{Tr}_i(\hat{\rho}_s^2)$, where $\hat{\rho}_s = \mathrm{Tr}_i(|\Psi\rangle\langle\Psi|)$ denotes the density operator of the heralded single photon, and Tr_i is the partial trace over the idler mode. Note that the heralded single-photon purity is given by $\mathrm{Tr}_i(\hat{\rho}_s^2) = K^{-1}$ [54]. For our QFCs, the single-photon purities are calculated to be 0.53, 0.61, and 0.65, respectively, indicating the emergence of high-purity quantum states.

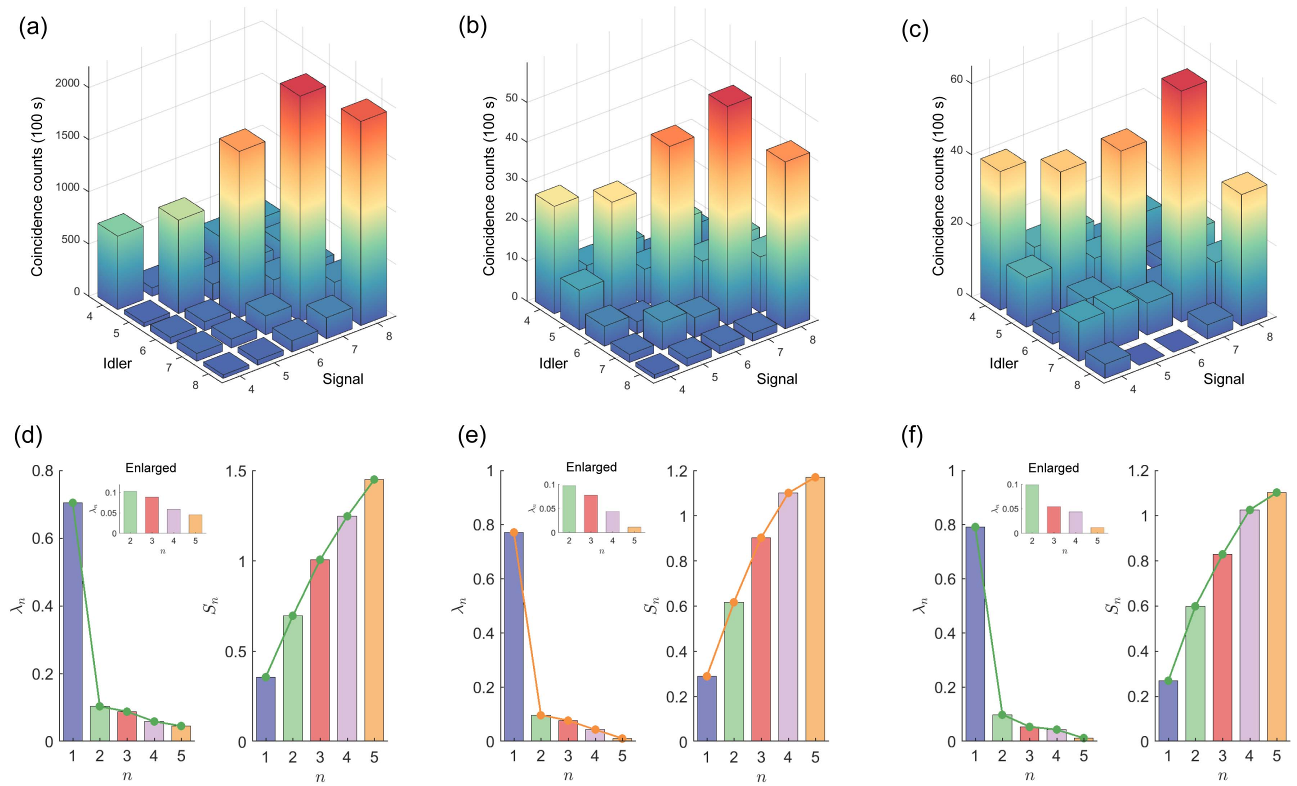

Fig. 4. Quantum properties of the QFCs detected at the outputs of the micro-resonator, straight, and Z-shaped topological waveguides. (a)–(c) Measured JSI distributions. (d)–(f) Distributions of normalized Schmidt coefficients λ_n and entanglement entropy S_k.

C. Topological Transport of DKS Combs

We also perform on-chip topological transport of DKS combs using the same Si_3N_4 micro-resonator. Before the experimental scheme, we numerically simulate the dynamic evolution of DKS combs described by the Lugiato–Lefever equation (LLE) (see Appendix F). However, accessing stable DKS combs in micro-resonators is challenging due to limitations imposed by laser tuning precision, frequency stability, and short thermal lifetime [53]. To address these challenges, we use a dual-pump method to extend the region of soliton existence (see Section 4). Also, the beat between the auxiliary and pump lasers could facilitate the generation of soliton crystals [56].

By scanning the pump laser from the blue to the red side of the resonator mode, one can clearly observe the comb evolution processes, including Turing rolls, chaotic states (breathing soliton states), multisoliton states, and single-soliton states [57]. Typically, a sharp decrease in intracavity power implies the arrival of a bistable state (referred to as a soliton step), which also demonstrates the arrival of a soliton state [53]. By stopping the pump laser scan at soliton step regions, DKS states can be easily accessed.

Figures 5(a)–5(c) show the measured optical spectra of the single-soliton states at the outputs of the micro-resonator, straight, and Z-shaped topological waveguides, respectively. These spectra show the smooth sech^2-shaped spectral envelope with a bandwidth of about 20 THz. The single-soliton spectrum also exhibits a 3 dB bandwidth of 29.3 nm, corresponding to a soliton pulse width of 87.5 fs. To further verify the noise performance of the single-soliton states, we use a CW laser to beat with one of the spectral lines of the combs. The resulting beat notes exhibit distinct frequency lines with resolution bandwidths (RBWs) of 100 kHz and signal-to-noise ratios of 30 dB (see Appendix H), indicating excellent low-noise characteristics.

Due to the inherently stochastic nature of intracavity dynamics, multisoliton states with a random soliton number N can be accessed during the frequency-tuning process [53]. The measured spectra of the multisoliton states in three cases are shown in Figs. 5(d)–5(f), where the spectrum of a multisoliton state is caused by interference among several solitons. As the number of solitons increases, the spectral characteristics become progressively more complex [57]. In other words, the intracavity solution for a multisoliton state can be described as the sum of several distinct, independent soliton solutions located at different positions. Interestingly, the adiabatic backward tuning method can effectively reduce the soliton number, allowing the transition from a multisoliton state to a single-soliton state [53].

We also access perfect soliton crystals using the forward tuning method with relatively low pump powers (100 mW). The formation of perfect soliton crystals results from the collective self-organization of multiple copropagating solitons. Figures 5(g)–5(i) show the measured spectra of perfect soliton crystals in three cases. The combs exhibit several evenly distributed supermodes separated by 13 FSRs, leading to a mode spacing of 1.24 THz. Additionally, our perfect soliton crystals can be regarded as a single soliton with a larger FSR, which can be used to generate ultra-high-repetition-rate DKS combs [58]. In the time domain, 13 DKSs with constant pulse separations of $2\pi/13$ are present in the resonator, reaching the maximum allowed number of solitons for the given pump. Since the comb power is distributed across 13 supermodes, the power of each supermode is amplified by a factor of 13^2, and the energy conversion efficiency is increased 13-fold compared to that of the single soliton state [57].

Benefiting from the large bandwidth of topological waveguides, we demonstrate the topological transport of DKS combs over a spectrum of approximately 20 THz. Remarkably, all DKS combs pass smoothly through sharp bends without

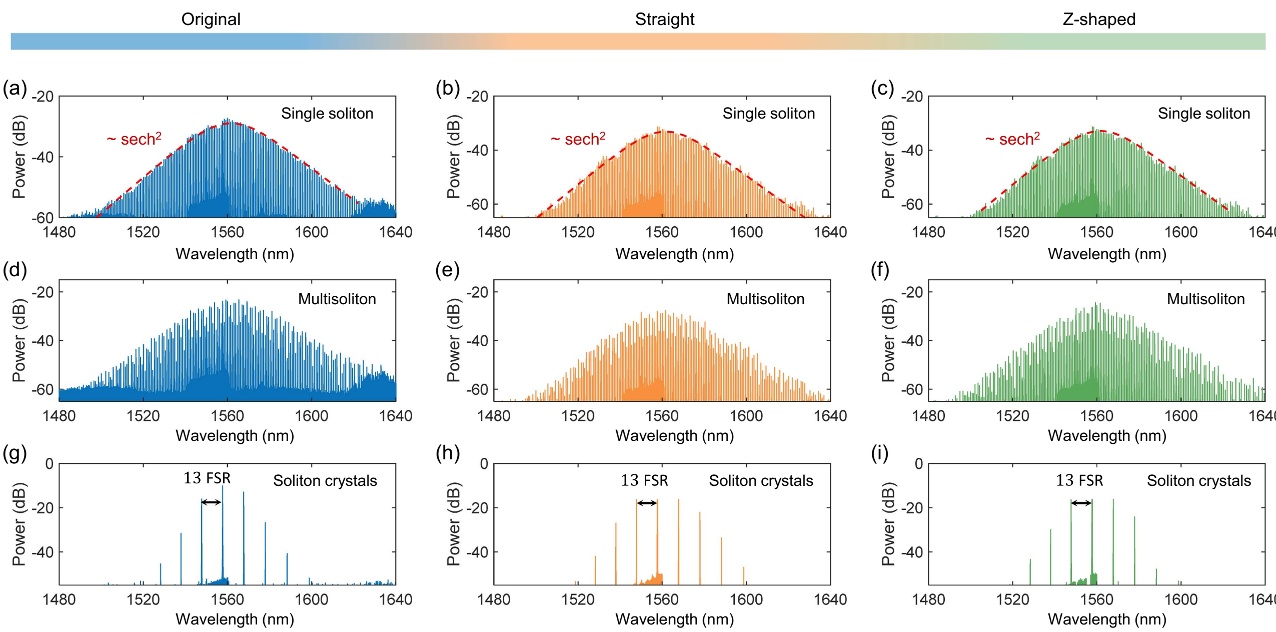

Fig. 5. Measured optical spectra of DKS combs at the outputs of the original micro-resonator, straight, and Z-shaped topological waveguides. (a)–(c) Single-soliton states. (d)–(f) Multisoliton states. (g)–(i) Perfect soliton crystals.

noticeable loss. Despite traveling through sharp turns, the DKSs retain their specific spectral envelope and low-noise characteristics, demonstrating the topological protection of soliton properties.

3. CONCLUSION

We have experimentally demonstrated the on-chip topological transport of QFCs and DKS combs at telecommunication wavelengths. In our fabricated VPC structures, we observe topologically protected kink states with a bandwidth of 25 THz. Using a Si_3N_4 micro-resonator, we access both frequency-entangled QFCs and mode-locked DKS combs. We show that the quantum correlations and frequency entanglement of high-dimensional quantum states exhibit no significant decoherence in the presence of structural perturbations, owing to the topological protection of the QVH effect. Furthermore, we demonstrate that mode-locked DKS combs retain their perfect spectral envelope and low-noise characteristics even after passing through topological interfaces. Topologically protected OFCs provide robust, complex, highly controllable, and scalable quantum resources, offering promising advances in quantum communication and information processing.

4. METHODS

A. Device Fabrication

We fabricate the topological devices on an SOI wafer with a 220 nm thick top silicon layer and 3 μm thick buried silicon layer. The edge coupler, silicon waveguide, and VPC structures are etched to a depth of 220 nm. We then deposit 1 μm thick SiO_2 cladding using plasma-enhanced chemical vapor deposition (PECVD). The entire chip is deeply etched and diced into multiple individual chips. The devices are fabricated using electron beam lithography (Vistec EBPG 5200+) and an inductively coupled plasma etching process (SPTS DRIE-I). For details on the fabrication process of the structures used in this work, see Refs. [59,60].

B. Experimental Setup for QFC Generation

In this experimental setup, we use a compact CW laser (Pure Photonics) with a wavelength of 1550.78 nm to pump the Si_3N_4 micro-resonator, and an EDFA to amplify the pump. Two cascaded bandpass filters are used to suppress the amplified spontaneous emission (ASE) noise generated by the EDFA. The power effectively coupled into the resonator is 6 mW. A temperature controller (TEC) is used to control the thermal instability of the mirco-resonator. The output QFC is coupled into topological waveguides after the polarization control. A 99:1 BS is connected to the output port, where 1% of the output power is detected by a programmable OPM (Joinwit) to monitor the pump power, allowing active control of the laser wavelength using a PID algorithm. The use of PID control ensures a stable resonant state for long-time coincidence measurement. The remaining 99% of the output power is filtered by an FBG, and the remaining QFCs are split by a 50:50 BS. The signal and idler modes are selected by two TBPFs (WL Photonics) with a bandwidth of 0.11 nm, and detected by two InGaAs SPDs (Aurea Technology).

For the JSI measurement, the SPDs are set to gated mode with a 20 MHz repetition rate, 20% quantum efficiency, and 10 μs dead time. The signals are then sent to a time analyzer to record coincidence events.

C. Experimental Setup for DKS Comb Generation

In this experimental setup, we use the dual-pump method to generate DKS combs by a computer-controlled soliton generation system [61]. The pump laser is excited by the same CW laser and amplified to 0.4 W by an EDFA. An additional auxiliary laser of 1 W power is used to stabilize the intracavity energy to extend the soliton steps. To reduce the crossed interaction of the two pumps, they are changed to orthogonal polarization modes by two independent FPCs. The two lasers are injected into the bus waveguide in opposite directions, with two circulators separating the input and residual pump light. The output comb is split by a 99:1 BS, with 1% of the output power detected by an OPM. The other 99% of the output power is split by a 90:10 BS, where 10% of the remaining power is sent to an OSA to measure the spectrum of the generated Kerr combs. After the polarization control, the remaining 90% of the residual output is coupled into the topological waveguides. The output of the topological waveguide is then sent to another OSA to monitor its spectrum.

In the computer-controlled soliton generation system, the auxiliary laser is tuned to the resonance wavelength to generate primary FWM sidebands. Note that the frequency modes of the pump laser and the FWM sidebands generated by the auxiliary laser are removed from the optical spectrum. The pump laser is automatically tuned from the blue to the red side to access the soliton states. The script assesses the intracavity state by monitoring the measured output power in the frequency-tuning process. Once the soliton state is accessed, the automation script gives the "stop" command for the pump laser (see Appendix D). In this case, the soliton state will hold for several hours.

D. Calculation of Heralded Efficiency for QFCs

We also calculate the heralded efficiency η_h, which is the probability of detecting an idler photon when the signal photon is detected. In general, the heralded efficiency can be given by $\eta_h = c_c/c_{\mathrm{signal}}\eta_{\mathrm{det}}$ [62], where c_c and c_{signal} are the coincidence and signal count rates, respectively, and η_{det} is the detection efficiency of the SPD for the idler mode (20%). Based on the obtained measurement, we derive a heralding efficiency of $\eta_h = 6\%$ without considering the losses of the experimental setup.

APPENDIX A: THEORY OF VPCS

For unperturbed unit cells exhibiting C_6 lattice symmetry, degenerate Dirac points occur at the K and K′ valleys. The effective Hamiltonian in the vicinity of the K (K′) point is given by [34,63,64]:

$$H_{K/K'} = \tau_z v_D(\sigma_x \delta k_x + \sigma_y \delta k_y), \tag{A1}$$

where v_D is the group velocity, σ_x and σ_y are the Pauli matrices, and $\delta\vec{k} = \vec{k} - \vec{k}_{K/K'}$ denotes the deviation of the wavevector. With the distortion of the unit cell ($d_1 \neq d_2$), the Hamiltonian can be rewritten as

$$H_{K/K'} = \tau_z v_D(\sigma_x \delta k_x + \sigma_y \delta k_y) + \tau_z \gamma \sigma_z, \quad \text{(A2)}$$

where $\tau_z = 1$ (−1) denotes the K (K′) valley pseudospin, $\sigma_{x,y,z}$ denotes the Pauli matrices, v_D is the group velocity, and γ is the strength of the symmetry-breaking perturbation. The perturbation is given by $\gamma_1 \propto (\int_B \varepsilon_z \mathrm{d}s - \int_A \varepsilon_z \mathrm{d}s)$ (VPC_1) and $\gamma_2 \propto (\int_D \boldsymbol{\varepsilon}_z \mathrm{d}s - \int_C \boldsymbol{\varepsilon}_z \mathrm{d}s)$ (VPC_2), where $\int \varepsilon_z ds$ is the integration of dielectric constant ε_z at the positions of A and B. In this context, the VPCs are $d_A = 0.72a_0$ and $d_B = 0.28a_0$, consequently leading to the inequality $\int_B \varepsilon_z \mathrm{d}s < \int_A \varepsilon_z \mathrm{d}s$. Additionally, we can get $|\gamma_1| > |\gamma_2|$. It indicates that the modes at the K and K′ valleys exhibit opposite circular polarizations, specifically, left-handed circular polarization (LCP) and right-handed circular polarization (RCP). The valley Chern numbers of VPCs can be given by [34,35]

$$C_{K/K'} = \frac{1}{2\pi} \int_{\mathrm{HBZ}} \Omega_{K/K'}(\delta\vec{k})\mathrm{d}S = \pm 1/2, \quad \text{(A3)}$$

where $\Omega = \nabla_k \times \vec{A}(k)$ is the Berry curvature, $\vec{A}(k)$ is the Berry connection, and this integration region contains half of the Brillouin zone. Hence, the disparity in the valley Chern numbers of the system is computed as $|C_{K/K'}| = 1$, confirming the topological characteristics of VPCs.

APPENDIX B: TOPOLOGICAL EDGE STATES

Topologically protected edge states in VPCs, also known as valley kink states [53], can be observed at the interfaces between VPC_1 and VPC_2. As shown by the red-dotted curve in Fig. 6(a), due to C_6 symmetry, a Dirac point appears at approximately $\lambda = 1566$ nm at the Brillouin zone corners (K and K′) where $d_1 = d_2 = 216$ nm. The inversion symmetry of the VPC can be broken by changing side lengths of triangular holes ($d_1 = 122$ nm and $d_2 = 295$ nm), which opens a bandgap as illustrated by the black-dotted curve in Fig. 6(a). To confirm the robustness of these edge states, we design a straight waveguide and a Z-shaped topological waveguide. The simulated field profiles of the valley kink states at the frequency of 193 THz (around 1550 nm) are shown in Figs. 6(c) and 6(d).

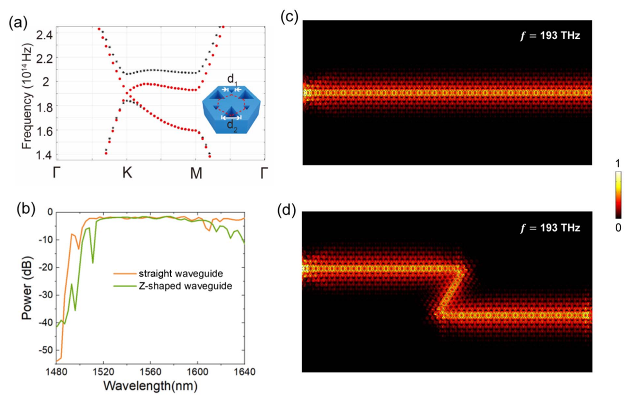

Fig. 6. (a) Band diagram of the VPC slab with inversion symmetry (red-dotted curves) compared with inversion symmetry breaking (black-diamond curves), where Γ, K, and M denote the high-symmetry points in the first Brillouin zone. (b) Simulated transmission spectra of the straight interface (orange curve) and Z-shaped interface (green curve). (c), (d) Simulated field profiles of the valley kink states at the frequency of 193 THz (around 1550 nm) at different interfaces.

The results reveal that valley kink states are highly centralized at the interfaces, and show robustness against sharp corners. The simulated transmission spectra of the straight interface and Z-shaped interface are shown in Fig. 6(b), revealing a topological bandgap from 1490 to 1640 nm. Such simulation results are consistent with the experiment result [Fig. 1(e)]. Note that for the edge states with wavelengths far away from the K point, there may exist random Anderson-localized cavities caused by coherent backscattering [65]. Since the potential cavities fall outside the scope of our manuscript, we will not delve into further discussion in this article.

APPENDIX C: MICRO-RESONATOR CHARACTERIZATION

We utilize a Si_3N_4 micro-resonator to generate both QFCs and DKS combs. Consequently, dispersion engineering becomes a critical manipulation for producing predictive combs in the micro-resonator. The waveguide cross-section is numerically simulated using the COMSOL Multiphysics software. In this context, we select a waveguide cross-section with $W = 1.8$ μm, $H = 0.8$ μm, and $\theta = 89°$. A schematic of the waveguide structure is presented in the inset of Fig. 7(b). A bus waveguide is used to couple the pump to the micro-resonator with a gap of 0.45 μm.

To generate both QFCs and DKS combs, it is necessary to design the micro-resonator with anomalous group-velocity dispersion (GVD). By expanding the propagation phase constant β in Taylor series, we can estimate the second term β_2 by

$$\beta_2 = \frac{1}{c}\left(2n\frac{\mathrm{d}n(\omega)}{\mathrm{d}\omega} + \omega\frac{\mathrm{d}^2 n(\omega)}{\mathrm{d}\omega^2}\right), \quad \text{(C1)}$$

where $n(\omega)$ signifies the effective refractive index. Figure 7(b) illustrates the simulated GVD curve for fundamental modes with transverse-electric (TE) and transverse-magnetic (TM) polarizations. It suggests a near-zero anomalous GVD around the wavelength of 1550 nm. Additionally, the corresponding mode profiles of TE and TM modes are depicted in Fig. 7(c). Following a meticulous design of the Si_3N_4 micro-resonator, we entrust the LIGETEC to fabricate resonators with the AN800 technology. A microscopy image of the Si_3N_4 micro-ring is presented in Fig. 7(a).

To measure the transmission spectrum of the micro-resonator, a tunable semiconductor laser (TSL, Santec) is swept from 1510 to 1590 nm. The result is illustrated in Fig. 8(a),

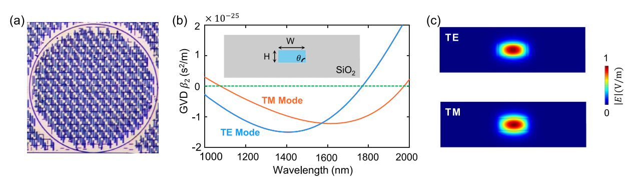

Fig. 7. (a) Microscopy image of the Si_3N_4 micro-ring with $W = 1.8$ μm, $H = 0.8$ μm, $\theta = 89°$, and gap width of 0.45 μm. (b) Simulated GVD curves for TE and TM modes, where the inset denotes a diagram of the waveguide cross-section. (c) Simulated mode profiles of TE and TM modes.

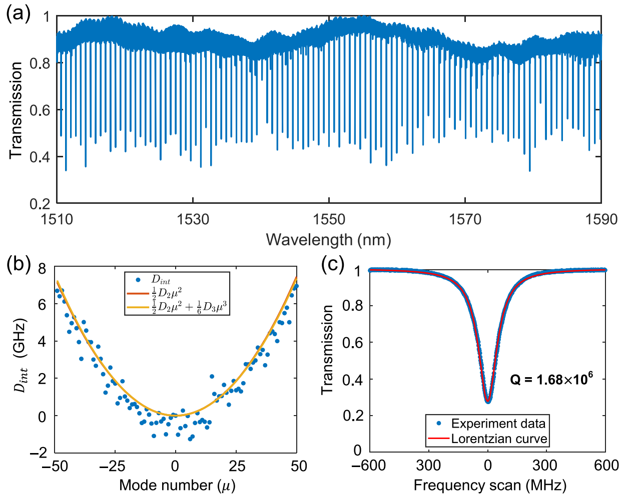

Fig. 8. (a) Measured transmission spectrum of the Si_3N_4 micro-resonator. (b) Dispersions of the micro-resonator extracted from the measured transmission. (c) Lorentzian fitting of the resonant dip.

which leads to an FSR of 95.75 GHz. The Taylor expansion for the cavity resonant mode ω_μ is expressed by

$$\omega_\mu = \omega_0 + \sum_{n=1}^{\infty} D_n \frac{\mu^n}{n!}, \tag{C2}$$

where μ ($\mu \in \mathbb{Z}$) denotes the mode indexing, and ω_0 corresponds to the pumped resonant mode. The expansion terms (also referred to as the high-order dispersion) can be written as $D_n = \mathrm{d}^n\omega_\mu/\mathrm{d}\mu^n$ at $\omega = \omega_0$. Another term, so-called integrated dispersion, is used to describe the resonator properties, which is given by $D_{\mathrm{int}}(\mu) = \omega_\mu - (\omega_0 + \mu D_1)$. Figure 8(b) shows dispersions of the micro-resonator extracted from the measured transmission, indicating a value of the second-order dispersion $D_2 = 5.95 \times 10^6$ rad/s. The appearance of resulting OFCs (both classic and quantum) depends on the quality factor (Q-factor) of micro-resonators. The total Q-factor is given by $1/Q = 1/Q_{\mathrm{in}} + 1/Q_{\mathrm{ex}}$, in which Q_{in} and Q_{ex} are the intrinsic quality factor and external quality factor, respectively. Here we sweep a resonant dip with a narrower linewidth at the pump wavelength. The Lorentzian fitting of the resonant dip shown in Fig. 8(c) reveals $Q_{\mathrm{in}} = 2.20 \times 10^6$ and $Q_{\mathrm{ex}} = 7.10 \times 10^6$. Hence, the total quality of the micro-resonator is calculated to be $Q = 1.68 \times 10^6$. And the loss can be calculated as $\kappa = 7.22 \times 10^8$ rad/s, $\kappa_{\mathrm{in}} = 5.51 \times 10^8$ rad/s, and $\kappa_{\mathrm{ex}} = 1.71 \times 10^8$ rad/s, respectively. Consequently, the coupling efficiency is determined as $\eta = \kappa_{\mathrm{ex}}/(\kappa_{\mathrm{ex}} + \kappa_{\mathrm{in}}) = 0.24$. This value indicates that the Si_3N_4 micro-ring, featuring a gap of 0.45 μm, corresponds to an under-coupling case [53].

APPENDIX D: PROTOTYPE OF OPTICAL FREQUENCY COMBS

To downsize the generation system for QFCs and DKS combs, we have advanced our previous prototype [61] to establish compatibility for these applications. We focus on building a standalone microcomb source integrating all the necessary hardware into a 21.5 inch chassis to reduce possible off-board destabilization during the operation processing. Figure 9 shows our promoted microcomb generation prototype. Compared with our previous system, in this iteration, we optimize the generation setup for producing DKS combs with the dual-pump method, and QFCs with the single-pump excitation method. A TEC with a feedback controller is packaged at the bottom of Si_3N_4 chip; the precision of this temperature stabilization subsystem is 2 mK. Besides, we improve the concentration and stability of optical and electric circuit arrangement.

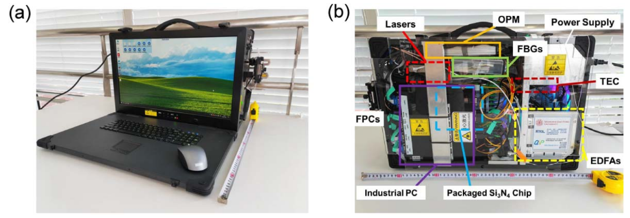

Fig. 9. Prototype for generating both QFCs and DKS combs.

We write corresponding scripts for the prototype's software to produce DKS combs and QFCs. In the case of DKS generation, the auxiliary laser is controlled to reach a resonant mode far away from the pump resonant wavelength automatically. The pump laser is tuned from the blue to the red side, and stops until the automation script discerns the soliton states according to the intracavity power. In the case of QFC generation, the frequency correlation measurement needs a stable resonant situation. To ensure this, we use a PID loop to actively control the pump laser's wavelength. In this script, once the pump laser accesses the resonant dip, the PID loop activates and stabilizes the output power.

APPENDIX E: THEORETICAL ANALYSIS OF QUANTUM FREQUENCY COMBS

Here we theoretically discuss the generation of QFCs in our Si_3N_4 resonators. The biphoton states are generated from a spontaneous FWM process, satisfying $2\omega_p = \omega_s + \omega_i$ and $2\vec{k}_p = \vec{k}_s + \vec{k}_i$, where $\omega_{p,s,i}$ and $\vec{k}_{p,s,i}$ are the frequencies and wavevectors of four photons. The nonlinear Hamiltonian of the FWM process in the resonator can be given by

$$H_{\mathrm{non}} = \frac{\chi^{(3)}}{2L}\int_{-L}^{0} \mathrm{d}z E_p^{(+)} E_p^{(+)} E_s^{(-)} E_i^{(-)} + \mathrm{h.c.}, \tag{E1}$$

where L is the cavity length, and h.c. denotes Hermitian conjugate. The pump field takes the form of a classical wave [66]:

$$E_p^{(+)}(z,t) = E_p e^{i(k_p z - \omega_p t)} e^{-i\Gamma P z}, \tag{E2}$$

where the term $e^{-i\Gamma P z}$ represents the pump self-phase modulation, Γ is the nonlinear parameter of Si_3N_4, and P is the intracavity power. In addition, the quantized field of signal and idler modes can be given by [66]

$$E_{s,i}^{(-)}(z,t) = \sqrt{\frac{\hbar\omega_{s,i}}{2\varepsilon_0 n_{s,i} c A_{\mathrm{eff}}}} \frac{\sqrt{\gamma_{s,i}\Delta\omega}}{2\pi} \sum_\mu \int_{-\infty}^{\infty} \mathrm{d}\Omega_{s,i} \times \frac{a_{s,i}^\dagger(\omega_{\mu_s,\mu_i} + \Omega_{s,i})}{\gamma_{s,i}/2 - i\Omega_{s,i}} e^{-i(k_{s,i}z - (\omega_{\mu_s,\mu_i} + \Omega_{s,i})t)}, \tag{E3}$$

where $\Delta\omega$ is the FSR, A_{eff} is effective field cross-section area, $\gamma_{s,i}$ is the linewidth of the cavity, ω_{μ_s,μ_i} is the μ-th central frequency with $\omega_{\mu_s,\mu_i} = \omega_p \pm \mu\Delta\omega$, and $\Omega_{s,i}$ denotes the deviation from ω_{μ_s,μ_i}. Therefore, the nonlinear Hamiltonian can be given by

$$H_{\text{non}} = \hbar\eta\sum_{\mu_s}\sum_{\mu_i}\int_{-\infty}^{\infty}\mathrm{d}\Omega_s\int_{-\infty}^{\infty}\mathrm{d}\Omega_i\frac{\sqrt{\gamma_s\gamma_i}F_{\mu_s,\mu_i}}{(\gamma_s/2 - i\Omega_s)(\gamma_i/2 - i\Omega_i)} \times a_s^\dagger(\omega_{\mu_s} + \Omega_s)a_i^\dagger(\omega_{\mu_i} + \Omega_i)e^{i((\mu_s+\mu_i)\Delta\omega+\Omega_s+\Omega_i)t} + \text{h.c.} \tag{E4}$$

Here, the constant term is

$$\eta = \frac{E_P^2}{16\pi^2\epsilon_0 cA_{\text{eff}}}\sqrt{\frac{\omega_s\omega_i}{n_s n_i}}\chi^{(3)}\Delta\omega. \tag{E5}$$

The interaction between signal and idler modes is

$$F_{\mu_s,\mu_i} = \int_{-L}^{0}\mathrm{d}z e^{i(2k_p - k_s - k_i - 2\Gamma P)}, \tag{E6}$$

where we can define the phase-matching condition term $\Delta k = 2k_p - k_s - k_i - 2\Gamma P$. Applying the first-order perturbation theory, the biphoton state can be calculated by

$$|\Psi\rangle = \frac{1}{i\hbar}\int_{-\infty}^{\infty}\mathrm{d}tH_{\text{non}}|0\rangle. \tag{E7}$$

In our resonators, the frequency deviation is much smaller than the FSR, that is, $|\Omega_{s,i}| \ll \Delta\omega_{s,i}$, and the index numbers of signal and idler modes are the same. Therefore we can get $\mu_s = \mu_i = \mu$ and $\Omega_s = -\Omega_i = \Omega$. Using these reasonable assumptions, the biphoton state can be simplified as

$$|\Psi\rangle = \eta\sum_{\mu}\int_{-\infty}^{\infty}\mathrm{d}\Omega\frac{\sqrt{\gamma_s\gamma_i}e^{i\Delta kL}}{(\gamma_s/2 - i\Omega)(\gamma_i/2 + i\Omega)} \times \text{sinc}(\Delta kL)a_s^\dagger(\omega_p - m\Delta\omega + \Omega)a_i^\dagger(\omega_p + m\Delta\omega - \Omega)|0\rangle. \tag{E8}$$

This equation describes the frequency correlation (as a result of energy conservation $2\omega_p = \omega_s + \omega_i$) of signal and idler photons. Furthermore, the comb-like biphoton state can be considered a discretized result of continuous frequency entanglement [55]. That is, the individual photon (a signal or idler photon) is a result of a superposition of hundreds of frequency modes, leading to a two-photon high-dimensional frequency-entangled state [15]. Specifically, a signal (idler) photon generated from spontaneous FWM could be found in any signal (idler) frequency modes $|\omega_p + \Omega\rangle$ ($|\omega_p - \Omega\rangle$). And their emergence at corresponding frequency modes is highly correlated. These QFCs are also proved to be frequency-bin entangled [16,17] and energy-time entangled [19].

Using Eq. (E8), we can assess the single-photon spectrum and JSI of generated QFCs. Generally, the single-photon spectrum of signal frequency modes can be given by [67]

$$S(\omega_s) = \langle\Psi|a_s^\dagger(\omega_s)a_s(\omega_s)|\Psi\rangle = \eta^2\sum_{\mu}\frac{\gamma_s\gamma_i\text{sinc}^2(i\Delta kL)}{|\gamma_s/2 - i(\omega_s - \omega_p + m\Delta\omega)|^2} \times \frac{1}{|\gamma_i/2 + i(\omega_s - \omega_p + m\Delta\omega)|^2}. \tag{E9}$$

This equation reveals that bandwidths of the single-photon spectrum are highly related to the phase-matching condition. A carefully designed dispersion may lead to a spectral bandwidth of 250 THz, ranging from near-ultraviolet to mid-infrared [68]. The generated frequency mode has a Lorentzian-like shape with a full width at half-maximum (FWHM) of $\sqrt{\sqrt{2}-1}\gamma \approx 0.64\gamma$, where we consider $\gamma_s = \gamma_1 = \gamma$. For our resonator, we can calculate a peak FWHM of 74 MHz for signal (idler) frequency mode, where the cavity linewidth is $\gamma = 115$ MHz.

Besides, we theoretically predict the JSI of generated QFCs by $\langle\Psi|a_s^\dagger(\omega_s)a_i^\dagger(\omega_i)a_s(\omega_i)a_i(\omega_i)|\Psi\rangle$. Therefore, the JSI can be given by

$$C_{\text{JSI}}(\mu) = \eta^2\int_{-\infty}^{\infty}\mathrm{d}\Omega\frac{\gamma_s\gamma_i}{(\gamma_s/2 - i\Omega)^2(\gamma_i/2 + i\Omega)^2}\text{sinc}^2(\Delta kL). \tag{E10}$$

Here, we can obtain these parameters from the transmission spectrum shown in Fig. 8(a), and ignore the term $2\Gamma P$. The normalized JSI of our Si_3N_4 resonator is plotted in Fig. 10(a). Here we consider signal-idler mode numbers from 4 to 40 (modes 1–3 are significantly eliminated by the FBG in the experiment).

To verify the frequency correlation of our biphoton frequency comb following the on-chip topological transport, we employ a coincidence count system to assess the JSI of QFCs. The entanglement exhibited by photon pairs can be elucidated by the factorizability of the JSA [55]. The JSA can be approximately obtained from the JSI by $\mathcal{A}(\omega_s,\omega_i) \approx \sqrt{|(\mathcal{A}(\omega_s,\omega_i)|^2}$. We employ Schmidt decomposition to validate the entanglement in the generated quantum frequency combs. If the biphoton state can be decomposed into a function of ω_s and ω_i, it signifies the presence of high-dimensional frequency entanglement. The JSA can be expressed as follows [55]:

$$\mathcal{A}(\omega_s,\omega_i) = \sum_{n=1}^{N}\sqrt{\lambda_n}\psi_n(\omega_s)\phi_n(\omega_i), \tag{E11}$$

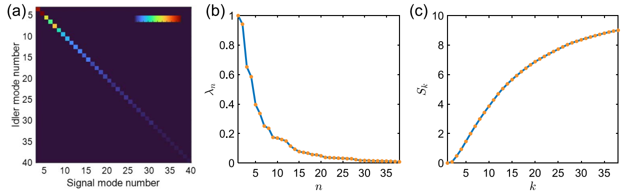

Fig. 10. (a) Simulated JSI of QFCs for the Si_3N_4 resonator. (b) Schmidt coefficients λ_n and (c) entropy of entanglement for the QFC.

where λ_n ($N \in \mathbb{N}$) is denoted as the Schmidt coefficient, and ψ_n and ϕ_n are orthonormal functions of ω_s and ω_i in the Hilbert space. λ_n, ψ_n, and ϕ_n are connected by these equations.

Subsequently, Eq. (E11) can be restructured as

$$\mathcal{A} = \sum_{n=1}^{N} \sqrt{\lambda_n}\psi_n\phi_n^T. \tag{E12}$$

With Eq. (E12), Schmit coefficients λ_n can be computed by solving the eigenvalue equations. Notably, when the count of non-zero Schmidt coefficients λ_n surpasses one, or when the entanglement entropy $S_k > 0$, the biphoton states exhibit frequency entanglement [55]. Moreover, the entropy of entanglement S_k and the Schmidt number K serve as effective measures for quantifying the entanglement:

$$S_k = -\sum_{n=1}^{N} \lambda_n \log_2 \lambda_n, \tag{E13}$$

$$K = \left(\sum_{n=1}^{N} \lambda_n\right)^2 / \sum_{n=1}^{N} \lambda_n^2. \tag{E14}$$

The entanglement of biphoton frequency combs is identified by $S_k > 0$ or $K > 1$; the large value of S_k and K leads to a high quality of high-dimensional frequency entanglement. For our Si_3N_4 resonator, the Schmidt number and entropy of entanglement are calculated as $K = 11.40$ and $S_k = 9$, respectively [Figs. 10(b) and 10(c)]. In the high-dimensional spaces, the Schmidt number K is an effective metric for quantifying the degree of entanglement between signal and idler modes. Therefore, the effective dimensions (numbers of relevant orthogonal modes) are larger than 11. However, the Schmidt number calculated from experimental data is not large enough because of the performance limitations of InGaAs SPDs. Due to its high-dimensional entanglement, QFCs have broad application prospects in quantum communication [69–71] and quantum computing [72,73].

APPENDIX F: NUMERICAL SIMULATION OF DKS COMBS

The LLE [74] describing the nonlinear evolution of the light field in micro-resonators can be given by the nonlinear Schrödinger equation (NSE)

$$\frac{\partial}{\partial z}A^{(m)} + \frac{\alpha}{2}A^{(m)} + i\frac{\beta_2}{2}\frac{\partial^2}{\partial T^2}A^{(m)} = ig_0|A^{(m)}|^2A^{(m)}, \tag{F1}$$

where $A^{(m)}$ is the field envelope for the m-th roundtrip, and L is length of the micro-resonator. The boundary condition can be written as

$$A^{(m+1)}(0,T) = \sqrt{\Theta}A_i + \sqrt{1-\Theta}\exp(-i\delta_0)A^{(m)}(L,T), \tag{F2}$$

where T represents the fast time variable that describes the waveform, A_i is the pump field, and Θ and δ_0 are the coupling coefficient and detuning of the resonance frequency, respectively. α, β_2, and g_0 are the roundtrip loss, second-order dispersion term, and nonlinear coefficient, respectively.

Assuming that the light field changes very little after a propagating distance of L, then $\partial/\partial z$ can be replaced by a slope with

$$\frac{\partial}{\partial z}A^{(m)}(z,T)|_{z=0} = \frac{A^{(m)}(L,T) - A^{(m)}(0,T)}{L}. \tag{F3}$$

The NSE gives how the light field changes when it travels a distance of L. Then we assume the power coupling coefficient is far smaller than one, that is, $\Theta \ll 1$, and the detuning is far smaller than FSR, that is, $\delta_0 \ll 2\pi$. We can rewrite Eq. (F2) as

$$A^{(m+1)}(0,T) = \sqrt{\Theta}A_i + \left(1 - \frac{\Theta}{2} - i\delta_0\right)A^{(m)}(L,T). \tag{F4}$$

To reduce the complexity of derivations, we replace the term m with slow time variable t_R. Therefore, we can obtain the relation

$$\frac{\partial}{\partial \tau}A(\tau,T) = \frac{A^{(m+1)}(0,T) - A^{(m)}(0,T)}{t_R}. \tag{F5}$$

We can rewrite Eq. (F5) with a new symbolic expression:

$$t_R\frac{\partial}{\partial \tau}A = -\left(\frac{\alpha L + \Theta}{2} + i\delta_0\right)A - iL\frac{\beta_2}{2}\frac{\partial^2}{\partial T^2}A + iLg_0|A|^2A + \sqrt{\Theta}A_i. \tag{F6}$$

This is the first form of LLE. Consequently, we replace several mathematical expressions to make the LLE more understandable. For example, the roundtrip time t_R can be calculated from the FSR of the resonator by $t_R = \frac{1}{\mathrm{FSR}}$, and the intrinsic loss and external loss can be expressed as $\kappa_{in} = \alpha L \cdot \mathrm{FSR}$ and $\kappa_{ex} = \Theta \cdot \mathrm{FSR}$, respectively. The total loss $\kappa = \kappa_{in} + \kappa_{ex}$ corresponds to the resonance linewidth. The normalized detuning is

$$\delta_0 = \beta_1 L(\omega_0 - \omega_p) = \frac{1}{\mathrm{FSR}}\delta\omega, \tag{F7}$$

where $\delta\omega$ is the detuning $\omega_0 - \omega_p$. The second-order dispersion and fast time variable T are

$$D_2 = -\frac{L}{2\pi}\beta_2(2\pi f_r)^3, \quad T = \frac{1}{2\pi f_r}\phi. \tag{F8}$$

Therefore, we can get the second form of LLE:

$$\frac{\partial}{\partial \tau}A = -\left(\frac{\kappa}{2} + i\delta\omega\right)A + i\frac{D_2}{2}\frac{\partial^2}{\partial \phi^2}A + iLf_r\gamma|A|^2A + \sqrt{f_r\kappa_{ex}}A_i, \tag{F9}$$

where τ is the slow time variable, and f_r is the FSR of the resonator. By using Eq. (F9), we can numerically simulate the nonlinear dynamic evolution of the Kerr solitons in our Si_3N_4 resonator. In our simulation, the pump power is set as 0.4 W, the FSR of the resonator is 95.75 GHz, the nonlinear index is 2.5×10^{-19} $m^2 W^{-1}$, the second-order dispersion is $D_2 = 5.95 \times 10^6$ rad/s, and the Q-factor is 1.68×10^6. We set a simulated effective field cross-section area at the pump wavelength by $A_{eff} = 2.1 \times 10^{-14}$ m^2, and therefore the nonlinear coefficient can be given by $g_0 = \omega_0 n_2 / cA_{eff}$.

The simulated intracavity energy and the corresponding spatiotemporal evolution of DKS combs as a function of the detuning are depicted in Figs. 11(a) and 11(b). We can clearly see several states, including stable modulation instability (SMI), chaotic modulation instability (CMI), breathing, and soliton states. The solitons always exist at the red-detuned side of

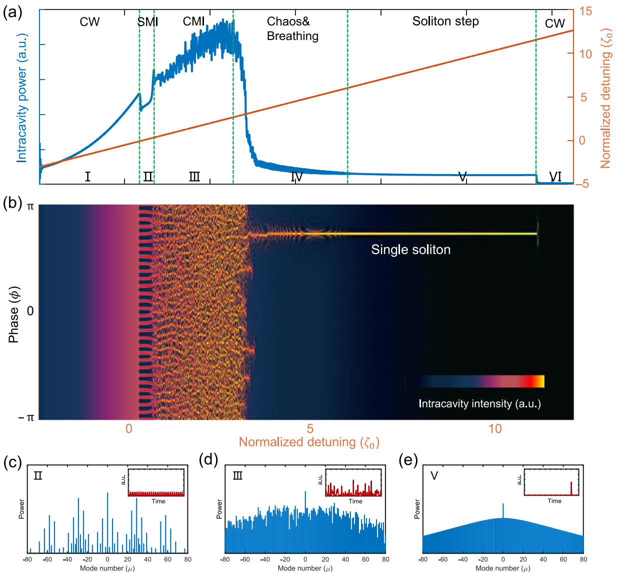

Fig. 11. Numerical simulation results of DKS combs evolution.

the resonance frequency, where the intracavity field is bistable. The simulated optical frequency combs are shown in Figs. 11(c)–11(e), which reveal the existence of a single-soliton state.

APPENDIX G: THEORETICAL ANALYSIS OF TOPOLOGICAL TRANSPORT OF SOLITONS

In this section, we study the evolution of soliton combs in VPC waveguides with certain dispersion. According to Eq. (F9), the temporal profile of the soliton can be written as $A(t) = A_0 \mathrm{sech}(\frac{t}{T_0})$, where A_0 and T_0 are the amplitude and pulse width of the soliton pulse. The evolution of solitons in photonic crystal waveguides is also governed by the NSE, which takes the form of [75]

$$i\frac{\partial A}{\partial z} + \frac{1}{v_g}\frac{\partial A}{\partial t} + \frac{\beta_2}{2}\frac{\partial^2 A}{\partial t^2} - ig_0|A|^2 A = 0, \qquad \textbf{(G1)}$$

where $v_g = \mathrm{d}\omega/\mathrm{d}k$ and β_2 are the group velocity and GVD, and g_0 is the nonlinear coefficient. By taking the derivative of edge dispersion of topological edge states [Fig. 1(b)], we can calculate the corresponding group velocity and GVD, as shown in Fig. 12(a). The dispersion of valley kink states is almost linear in the bandgap [34], so the GVD is relatively small.

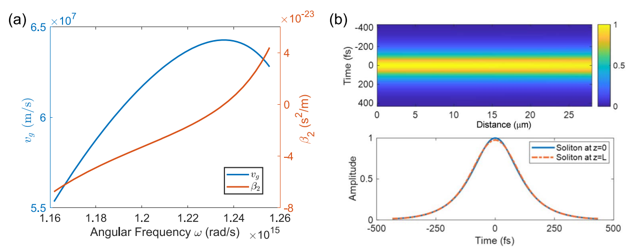

Fig. 12. (a) Calculated group velocity (v_g) and GVD (β_2) as a function of angular frequency. (b) Evolution of the single-soliton temporal profile along the propagation distance z.

Given the relatively low power of the single soliton (around 1 mW) and the short length of the photonic crystal waveguide (both the straight and Z-shaped topological waveguides are 28 μm), the nonlinear effect on soliton transmission is not included in this simulation. By solving Eq. (G1) with the split-step Fourier method, we can obtain the evolution of the soliton temporal profile along the propagation distance z. As shown in Fig. 12(b), the single-soliton envelope maintains a well-preserved shape during transmission, demonstrating the topological protection characteristic.

APPENDIX H: RF BEAT NOTES OF THE SINGLE-SOLITON COMB

To further characterize the performance of the single-soliton comb, a reference CW laser (TSL) is employed to generate a single-wavelength laser with a typical linewidth of 60 kHz. The output combs are heterodyned with a CW laser and then directed to a photodetector. The resulting electrical spectrum was measured with an electrical spectrum analyzer, as shown in Fig. 13. The RBWs are around 100 kHz. The signal-to-noise ratio was approximately 30 dB, indicating the presence of a narrow pulse width in this configuration of the single-soliton comb.

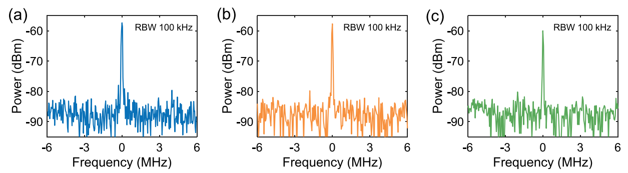

Fig. 13. RF beat notes of the single-soliton states for the (a) original DKS combs, and DKS combs after the transport of the (b) straight and (c) Z-shaped topological waveguides.

Funding. Key-Area Research and Development Program of Guangdong Province (2018B030325002); National Natural Science Foundation of China (62075129, 61975119, 62305210, 62035016, 62105200); Science and Technology on Metrology and Calibration Laboratory (JLKG2024001B002); SJTU Pinghu Institute of Intelligent Optoelectronics (2022SPIOE204).

Disclosures. The authors declare no conflicts of interest.

Data Availability. Data used in this study are available from the corresponding author upon reasonable request.

REFERENCES

1. M.-G. Suh and K. J. Vahala, "Soliton microcomb range measurement," Science **359**, 884–887 (2018).
2. P. Trocha, M. Karpov, D. Ganin, *et al.*, "Ultrafast optical ranging using microresonator soliton frequency combs," Science **359**, 887–891 (2018).
3. J. Riemensberger, A. Lukashchuk, M. Karpov, *et al.*, "Massively parallel coherent laser ranging using a soliton microcomb," Nature **581**, 164–170 (2020).

4. R. Chen, H. Shu, B. Shen, *et al.*, "Breaking the temporal and frequency congestion of LiDAR by parallel chaos," Nat. Photonics **17**, 306–314 (2023).
5. J. Pfeifle, V. Brasch, M. Lauermann, *et al.*, "Coherent terabit communications with microresonator Kerr frequency combs," Nat. Photonics **8**, 375–380 (2014).
6. A. Dutt, C. Joshi, X. Ji, *et al.*, "On-chip dual-comb source for spectroscopy," Sci. Adv. **4**, e1701858 (2018).
7. M. Yu, Y. Okawachi, A. G. Griffith, *et al.*, "Silicon-chip-based mid-infrared dual-comb spectroscopy," Nat. Commun. **9**, 1869 (2018).
8. D. T. Spencer, T. Drake, T. C. Briles, *et al.*, "An optical-frequency synthesizer using integrated photonics," Nature **557**, 81–85 (2018).
9. S.-W. Huang, J. Yang, M. Yu, *et al.*, "A broadband chip-scale optical frequency synthesizer at 2.7×10^{-16} relative uncertainty," Sci. Adv. **2**, e1501489 (2016).
10. J. Feldmann, N. Youngblood, M. Karpov, *et al.*, "Parallel convolutional processing using an integrated photonic tensor core," Nature **589**, 52–58 (2021).
11. X. Xu, M. Tan, B. Corcoran, *et al.*, "11 TOPS photonic convolutional accelerator for optical neural networks," Nature **589**, 44–51 (2021).
12. G. Moody, V. J. Sorger, D. J. Blumenthal, *et al.*, "2022 roadmap on integrated quantum photonics," J. Phys. Photonics **4**, 012501 (2022).
13. E. Pelucchi, G. Fagas, I. Aharonovich, *et al.*, "The potential and global outlook of integrated photonics for quantum technologies," Nat. Rev. Phys. **4**, 194–208 (2022).
14. M. Kues, C. Reimer, J. M. Lukens, *et al.*, "Quantum optical microcombs," Nat. Photonics **13**, 170–179 (2019).
15. M. Kues, C. Reimer, P. Roztocki, *et al.*, "On-chip generation of high-dimensional entangled quantum states and their coherent control," Nature **546**, 622–626 (2017).
16. P. Imany, J. A. Jaramillo-Villegas, O. D. Odele, *et al.*, "50-GHz-spaced comb of high-dimensional frequency-bin entangled photons from an on-chip silicon nitride microresonator," Opt. Express **26**, 1825–1840 (2018).
17. M. Clementi, F. A. Sabattoli, M. Borghi, *et al.*, "Programmable frequency-bin quantum states in a nano-engineered silicon device," Nat. Commun. **14**, 176 (2023).
18. N. Chen, W. Chi, Y. Fan, *et al.*, "Parity-time-symmetry-enabled broadband quantum frequency-comb generation," Phys. Rev. A **110**, 023714 (2024).
19. T. J. Steiner, J. E. Castro, L. Chang, *et al.*, "Ultrabright entangled-photon-pair generation from an AlGaAs-on-insulator microring resonator," PRX Quantum **2**, 010337 (2021).
20. J. A. Jaramillo-Villegas, P. Imany, O. D. Odele, *et al.*, "Persistent energy-time entanglement covering multiple resonances of an on-chip biphoton frequency comb," Optica **4**, 655–658 (2017).
21. Y.-R. Fan, C. Lyu, C.-Z. Yuan, *et al.*, "Multi-wavelength quantum light sources on silicon nitride micro-ring chip," Laser Photonics Rev. **17**, 2300172 (2023).
22. H. Zeng, Z.-Q. He, Y.-R. Fan, *et al.*, "Quantum light generation based on GaN microring toward fully on-chip source," Phys. Rev. Lett. **132**, 133603 (2024).
23. R. Chen, Y.-H. Luo, J. Long, *et al.*, "Ultralow-loss integrated photonics enables bright, narrowband, photon-pair sources," Phys. Rev. Lett. **133**, 083803 (2024).
24. C. Reimer, M. Kues, P. Roztocki, *et al.*, "Generation of multiphoton entangled quantum states by means of integrated frequency combs," Science **351**, 1176–1180 (2016).
25. N. T. Islam, C. C. W. Lim, C. Cahall, *et al.*, "Provably secure and high-rate quantum key distribution with time-bin qudits," Sci. Adv. **3**, e1701491 (2017).
26. P. Imany, J. A. Jaramillo-Villegas, M. S. Alshaykh, *et al.*, "High-dimensional optical quantum logic in large operational spaces," NPJ Quantum Inf. **5**, 59 (2019).
27. A. Omran, H. Levine, A. Keesling, *et al.*, "Generation and manipulation of Schrödinger cat states in Rydberg atom arrays," Science **365**, 570–574 (2019).
28. T. Dai, Y. Ao, J. Bao, *et al.*, "Topologically protected quantum entanglement emitters," Nat. Photonics **16**, 248–257 (2022).
29. F. D. M. Haldane and S. Raghu, "Possible realization of directional optical waveguides in photonic crystals with broken time-reversal symmetry," Phys. Rev. Lett. **100**, 013904 (2008).
30. S. Raghu and F. D. M. Haldane, "Analogs of quantum-hall-effect edge states in photonic crystals," Phys. Rev. A **78**, 033834 (2008).
31. X. Cheng, C. Jouvaud, X. Ni, *et al.*, "Robust reconfigurable electromagnetic pathways within a photonic topological insulator," Nat. Mater. **15**, 542–548 (2016).
32. L.-H. Wu and X. Hu, "Scheme for achieving a topological photonic crystal by using dielectric material," Phys. Rev. Lett. **114**, 223901 (2015).
33. A. Slobozhanyuk, S. H. Mousavi, X. Ni, *et al.*, "Three-dimensional all-dielectric photonic topological insulator," Nat. Photonics **11**, 130–136 (2017).
34. Y. Yang, Y. Yamagami, X. Yu, *et al.*, "Terahertz topological photonics for on-chip communication," Nat. Photonics **14**, 446–451 (2020).
35. M. I. Shalaev, W. Walasik, A. Tsukernik, *et al.*, "Robust topologically protected transport in photonic crystals at telecommunication wavelengths," Nat. Nanotechnol. **14**, 31–34 (2019).
36. H. Wang, L. Sun, Y. He, *et al.*, "Asymmetric topological valley edge states on silicon-on-insulator platform," Laser Photonics Rev. **16**, 2100631 (2022).
37. X.-T. He, E.-T. Liang, J.-J. Yuan, *et al.*, "A silicon-on-insulator slab for topological valley transport," Nat. Commun. **10**, 872 (2019).
38. J. W. You, Z. Lan, and N. C. Panoiu, "Four-wave mixing of topological edge plasmons in graphene metasurfaces," Sci. Adv. **6**, eaaz3910 (2020).
39. D. Smirnova, S. Kruk, D. Leykam, *et al.*, "Third-harmonic generation in photonic topological metasurfaces," Phys. Rev. Lett. **123**, 103901 (2019).
40. S. S. Kruk, W. Gao, D.-Y. Choi, *et al.*, "Nonlinear imaging of nanoscale topological corner states," Nano Lett. **21**, 4592–4597 (2021).
41. S. Mittal, E. A. Goldschmidt, and M. Hafezi, "A topological source of quantum light," Nature **561**, 502–506 (2018).
42. Z. Jiang, Y. Ding, C. Xi, *et al.*, "Topological protection of continuous frequency entangled biphoton states," Nanophotonics **10**, 4019–4026 (2021).
43. Z. Jiang, C. Xi, G. He, *et al.*, "Topologically protected energy-time entangled biphoton states in photonic crystals," J. Phys. D **55**, 315104 (2022).
44. S. Mittal, G. Moille, K. Srinivasan, *et al.*, "Topological frequency combs and nested temporal solitons," Nat. Phys. **17**, 1169–1176 (2021).
45. Z. Jiang, L. Zhou, W. Li, *et al.*, "Topological dissipative Kerr soliton combs in a valley photonic crystal resonator," Phys. Rev. B **108**, 205421 (2023).
46. Z. Jiang, Y. Chen, C. Jiang, *et al.*, "Generation of quantum optical frequency combs in topological resonators," Adv. Quantum Technol. **7**, 2300354 (2024).
47. C. J. Flower, M. J. Mehrabad, L. Xu, *et al.*, "Observation of topological frequency combs," Science **384**, 1356–1361 (2024).
48. S. Mittal, V. V. Orre, E. A. Goldschmidt, *et al.*, "Tunable quantum interference using a topological source of indistinguishable photon pairs," Nat. Photonics **15**, 542–548 (2021).
49. Y. Chen, X.-T. He, Y.-J. Cheng, *et al.*, "Topologically protected valley-dependent quantum photonic circuits," Phys. Rev. Lett. **126**, 230503 (2021).
50. L. He, D. Liu, H. Zhang, *et al.*, "Topologically protected quantum logic gates with valley-hall photonic crystals," Adv. Mater. **36**, 2311611 (2024).
51. S. Arora, T. Bauer, R. Barczyk, *et al.*, "Direct quantification of topological protection in symmetry-protected photonic edge states at telecom wavelengths," Light Sci. Appl. **10**, 9 (2021).
52. H. Wang, G. Tang, Y. He, *et al.*, "Ultracompact topological photonic switch based on valley-vortex-enhanced high-efficiency phase shift," Light Sci. Appl. **11**, 292 (2022).
53. T. J. Kippenberg, A. L. Gaeta, M. Lipson, *et al.*, "Dissipative Kerr solitons in optical microresonators," Science **361**, eaan8083 (2018).
54. L. E. Vicent, A. B. U'Ren, R. Rangarajan, *et al.*, "Design of bright, fiber-coupled and fully factorable photon pair sources," New J. Phys. **12**, 093027 (2010).

55. C. Law, I. A. Walmsley, and J. Eberly, “Continuous frequency entanglement: effective finite hilbert space and entropy control,” Phys. Rev. Lett. **84**, 5304–5307 (2000).
56. W. Wang, L. Wang, and W. Zhang, “Advances in soliton microcomb generation,” Adv. Photonics **2**, 034001 (2020).
57. V. Brasch, M. Geiselmann, T. Herr, *et al.*, “Photonic chip–based optical frequency comb using soliton Cherenkov radiation,” Science **351**, 357–360 (2016).
58. M. Karpov, M. H. Pfeiffer, H. Guo, *et al.*, “Dynamics of soliton crystals in optical microresonators,” Nat. Phys. **15**, 1071–1077 (2019).
59. Y. Su and Y. Zhang, *Passive Silicon Photonics Devices* (American Institute of Physics, 2022).
60. Y. Su, Y. Zhang, C. Qiu, *et al.*, “Silicon photonic platform for passive waveguide devices: materials, fabrication, and applications,” Adv. Mater. Technol. **5**, 1901153 (2020).
61. L. Zhou, Y. Shen, C. Xi, *et al.*, “Computer-controlled microresonator soliton comb system automating soliton generation and expanding excursion bandwidth,” Opt. Contin. **1**, 161–170 (2022).
62. K. Zielnicki, K. Garay-Palmett, D. Cruz-Delgado, *et al.*, “Joint spectral characterization of photon-pair sources,” J. Mod. Opt. **65**, 1141–1160 (2018).
63. J. Lu, C. Qiu, L. Ye, *et al.*, “Observation of topological valley transport of sound in sonic crystals,” Nat. Phys. **13**, 369–374 (2017).
64. J. Noh, S. Huang, K. P. Chen, *et al.*, “Observation of photonic topological valley hall edge states,” Phys. Rev. Lett. **120**, 063902 (2018).
65. C. A. Rosiek, G. Arregui, A. Vladimirova, *et al.*, “Observation of strong backscattering in valley-Hall photonic topological interface modes,” Nat. Photonics **17**, 386–392 (2023).
66. M. Scholz, L. Koch, and O. Benson, “Analytical treatment of spectral properties and signal–idler intensity correlations for a double-resonant optical parametric oscillator far below threshold,” Opt. Commun. **282**, 3518–3523 (2009).
67. J. Chen, Z. H. Levine, J. Fan, *et al.*, “Frequency-bin entangled comb of photon pairs from a silicon-on-insulator micro-resonator,” Opt. Express **19**, 1470–1483 (2011).
68. X. Lu, Q. Li, D. A. Westly, *et al.*, “Chip-integrated visible–telecom entangled photon pair source for quantum communication,” Nat. Phys. **15**, 373–381 (2019).
69. F. Xu, X. Ma, Q. Zhang, *et al.*, “Secure quantum key distribution with realistic devices,” Rev. Mod. Phys. **92**, 025002 (2020).
70. S. Liang, J. Cheng, J. Qin, *et al.*, “High-speed quantum radio-frequency-over-light communication,” Phys. Rev. Lett. **132**, 140802 (2024).
71. Y. Tian, P. Wang, J. Liu, *et al.*, “Experimental demonstration of continuous-variable measurement-device-independent quantum key distribution over optical fiber,” Optica **9**, 492–500 (2022).
72. H.-S. Zhong, H. Wang, Y.-H. Deng, *et al.*, “Quantum computational advantage using photons,” Science **370**, 1460–1463 (2020).
73. S. Cao, B. Wu, F. Chen, *et al.*, “Generation of genuine entanglement up to 51 superconducting qubits,” Nature **619**, 738–742 (2023).
74. L. A. Lugiato and R. Lefever, “Spatial dissipative structures in passive optical systems,” Phys. Rev. Lett. **58**, 2209–2211 (1987).
75. P. Colman, C. Husko, S. Combrié, *et al.*, “Temporal solitons and pulse compression in photonic crystal waveguides,” Nat. Photonics **4**, 862–868 (2010).